JGR Atmospheres

RESEARCH ARTICLE
10.1029/2024JD041948

Boreal Winter Hadley Cell Contraction in Response to the Incorporation of a Comprehensive Ocean Surface Albedo in CESM2

Jian Wei[1], **Ping Yang**[1,2,3], **and Qiang Fu**[4]

[1]Department of Atmospheric Sciences, Texas A&M University, College Station, TX, USA, [2]Department of Oceanography, Texas A&M University, College Station, TX, USA, [3]Department of Physics and Astronomy, Texas A&M University, College Station, TX, USA, [4]Department of Atmospheric and Climate Sciences, University of Washington, Seattle, WA, USA

Key Points:

- The El Niño-like warming pattern due to considering ocean surface albedo physics comprehensively is demonstrated
- Equatorward shift in temperature gradients alters eddy momentum flux, limits meridional winds, and contracts the Hadley Cell (HC)
- A scaling theory supports HC contraction with stronger subtropical zonal winds, enhancing angular momentum and limiting its extent

Supporting Information:

Supporting Information may be found in the online version of this article.

Correspondence to:

J. Wei,
anser@tamu.edu

Citation:

Wei, J., Yang, P., & Fu, Q. (2024). Boreal winter Hadley Cell contraction in response to the incorporation of a comprehensive ocean surface albedo in CESM2. *Journal of Geophysical Research: Atmospheres*, *129*, e2024JD041948. https://doi.org/10.1029/2024JD041948

Received 8 JUL 2024
Accepted 24 NOV 2024

Author Contributions:

Conceptualization: Jian Wei
Data curation: Jian Wei
Formal analysis: Jian Wei, Ping Yang, Qiang Fu
Funding acquisition: Ping Yang, Qiang Fu
Investigation: Jian Wei
Methodology: Jian Wei, Ping Yang, Qiang Fu
Project administration: Ping Yang, Qiang Fu
Resources: Jian Wei
Supervision: Ping Yang, Qiang Fu
Visualization: Jian Wei
Writing – original draft: Jian Wei

Abstract This study investigates the causes of shifts in the subsiding edge of the boreal winter Hadley cell (HC) in response to a comprehensive treatment of ocean surface albedo (OSA) in the fully coupled CESM2. The focus is on an in-depth understanding of the atmospheric dynamical processes that influence the HC subsiding edge. Two sets of experiments were performed: one utilizing the default OSA, and the other employing the comprehensive OSA that accounts for realistic physical mechanisms. The results show that implementing the comprehensive OSA simulates an El Niño-like warming pattern in reference to the default experiment, which leads to an HC contraction. Examination of zonal mean momentum dynamics in the upper troposphere reveals that variations in meridional winds, crucial for determining the HC extent, are primarily driven by the differences in the horizontal eddy momentum flux derivative. The findings indicate that the equatorward shift in meridional temperature gradients enhances subtropical zonal winds and baroclinicity along their equatorial flanks, amplifying equatorward-propagating Rossby waves. This, in turn, alters the eddy momentum flux, reshaping the pattern of the derivatives of horizontal eddy momentum flux, constraining meridional winds, and resulting in the equatorward movement of the HC subsiding edge. A scaling theory further supports the results of the HC contraction, showing that the increased subtropical zonal winds and the equatorward shift of the Intertropical Convergence Zone (ITCZ) elevate the atmospheric angular momentum and eventually limit the expansion of the HC.

Plain Language Summary The Hadley cell (HC) is a large-scale tropical circulation system that exerts a substantial influence on global and regional climates. However, it is necessary to further explain the mechanisms that control the HC edge. This study investigates how the HC descending edge shifts when a comprehensive ocean surface albedo (OSA), including more realistic physical processes, is used in a fully coupled climate model. Two sets of simulations were conducted: one using the default OSA, which neglects certain physical processes, and the other using the comprehensive OSA. The comprehensive OSA experiment simulated an El Niño-like warming climate in contrast to the default simulation, with equatorward movement of the HC edge. The present study finds that the equatorward shift in the air meridional temperature gradient results in the intensification of the subtropical zonal winds and baroclinic instability along their equatorial flanks, enhancing equatorward Rossby wave activities and affecting the pattern of the horizontal eddy momentum flux. This constrains the meridional winds, causing the HC edge to move equatorward. A scaling theory supports these findings by showing that the stronger subtropical winds and the equatorward shift of the Intertropical Convergence Zone (ITCZ) increase the atmospheric angular momentum and subsequently prevent the HC expanding.

1. Introduction

A crucial feature of the Earth's climate is the poleward transport of energy needed to compensate for an equatorial energy surplus and high-latitude deficit caused by differential solar heating (e.g., Webb, 2019). The Hadley cell (HC), consisting of two counter-rotating cells near the equator, dominates the atmospheric circulation in the tropics. Low-level atmospheric heat and moisture from the Northern Hemisphere (NH) and Southern Hemisphere (SH) converge into the Intertropical Convergence Zone (ITCZ), where this warm moist air rises into the upper troposphere and flows poleward in both hemispheres, forcing downdrafts of dry air in the subtropics (Trenberth & Stepaniak, 2003). The latitudes of these descending currents, or the HC subsiding edges, mark the boundaries of

Writing – review & editing: Jian Wei, Ping Yang, Qiang Fu

Earth's tropical belt (e.g., Davis & Birner, 2017), which vary seasonally and interannually in response to climate forcings. Any such change in the width of the tropics has the potential to exert various impacts on regional and global climate (e.g., Seidel et al., 2008; Staten et al., 2018).

Previous studies suggest that the HC subsiding edges have been moving poleward over the last several decades in response to global warming based upon a wide range of metrics using observations, reanalysis products, and a suite of climate model simulations under different historical and future projected scenarios (e.g., Choi et al., 2014; Fu et al., 2006; Grise & Davis, 2020; Hu et al., 2011, 2018; Hu & Fu, 2007; Kang & Lu, 2012; Lau & Kim, 2015; Lau & Tao, 2020; Lionello et al., 2024; Lu et al., 2008; Lucas et al., 2014; Seidel et al., 2008; Seidel & Randel, 2007; Staten et al., 2018; Watt-Mayer et al., 2019; Yang et al., 2020). To disentangle the causes of the HC subsiding edge shifts, several theories were proposed based on different thermodynamic considerations. For instance, the HC extent has been quantitatively discussed in scaling relations under the assumption of mean angular momentum conservation in the tropics (Held, 2000; Held & Hou, 1980; Kang & Lu, 2012), and is linked to variations in static stability, the meridional air temperature gradient, tropopause height and the location of the ITCZ in a wide range of dry and moist idealized general circulation model (GCM) studies (Chemke & Polvani, 2019; Hilgenbrink & Hartmann, 2018; Korty & Schneider, 2008; Lu et al., 2007; Seo et al., 2014). However, scaling is built on the conception of the HC being thermally forced, which is only intended for highlighting the most essential or dominant dynamical factors in the tropics and subtropics that can contribute to HC expansion under global warming (Kang & Lu, 2012; Kim & Lee, 2001). Extratropical processes (excluded in the scaling) could also play important roles in adjusting the geographical HC configuration (Chemke et al., 2019; Deser et al., 2015; England et al., 2020; Kang, 2020; Kang et al., 2020, 2023; Kim et al., 2022; Lu et al., 2008). In addition, angular momentum is not entirely conserved (Schneider, 2006; Walker & Schneider, 2006), especially near subtropical HC boundaries where eddy activities dominate. It is also found that subtropical baroclinicity, and Rossby wave propagations and breaks, are associated with displacements of the HC edges (Homeyer & Bowman, 2013; Lu et al., 2008; Tandon et al., 2013; Walker & Schneider, 2006; Wittman et al., 2007). Multiple causes mentioned here may operate concurrently. HC contraction (the subsiding edge moving equatorward), as observed in El Niño events (e.g., Adam et al., 2014) or occurring under El Niño-like warming simulations in idealized or fully coupled GCMs (e.g., Lu et al., 2008; Tandon et al., 2013; Xie et al., 2022), has been documented, which were found to be strongly related to the zonal mean meridional temperature gradient (Adam et al., 2014; Davis & Birner, 2013; Levine & Schneider, 2015; Lu et al., 2008; Nguyen et al., 2013; Seager et al., 2003; Stachnik & Schumacher, 2011). However, few studies detailed the dynamic processes involved in the equatorward movement of the HC subsiding edge associated with the El Niño-like warming pattern. Because of the complex nature of the climate system, the underlying physical dynamical mechanisms controlling the HC border are still partly unclear (Staten et al., 2018).

The importance of the sea surface temperature (SST) and its pattern in controlling the HC fringe is well established (e.g., Chemke & Polvani, 2018; Chen et al., 2013; Feng et al., 2019; Hilgenbrink & Hartmann, 2018; Knietzsch et al., 2015; Li et al., 2023; Nguyen et al., 2013; Rollings & Merlis, 2021; Yang et al., 2020; Zhou et al., 2020). Because the ocean surface is the major atmospheric boundary, any differences in ocean surface thermodynamics would affect heat flux transport at the air-sea interface in the coupled atmosphere-ocean system (e.g., Chemke & Polvani, 2018). This demonstrates the significant role of the ocean surface albedo (OSA; defined as the ratio of the upward irradiance to the incoming solar irradiance at the sea surface), which not only regulates the amount of radiation penetrating into the upper ocean but also determines the quantity of solar energy reflected back. Consequently, OSA is crucial in energy redistribution and subsequently in driving-related dynamic circulations (Hall, 2004). However, almost all current GCM simulations calculate OSA in a highly simplified way (Wei et al., 2021). Modeling of OSA in GCMs generally neglects several physical mechanisms, specifically light absorption beneath the sea surface induced by oceanic optical constituents and upward scattered of light that subsequently refracts back to the atmosphere through the sea-air boundary (referred to as water-leaving radiation), as well as the reflection of light by sea surface whitecaps. Simulated energy flows neglecting the above factors in the computation of OSA would reshape the energy budget across the coupled atmosphere-ocean framework and may have an impact on simulated SST and its pattern.

Therefore, there is a great interest in investigating the movement of the HC subsiding edge, by replacing the current oversimplified OSA treatment with a comprehensive OSA depiction in the fully coupled model. This inspires the present work to explore the atmospheric dynamical processes in detail, which govern the displacement of the temporal and zonal mean HC subsiding edge, in response to the implementation of a comprehensive

OSA to account for the physical mechanisms more realistically, within a fully coupled GCM. This study is organized as follows. Section 2 outlines the model, experiments, and HC edge metric used. Section 3 discusses the simulated results. Section 4 provides a summary and discussion.

2. Methods

2.1. Model and Experiments

To investigate the effects of implementing the comprehensive OSA on the movement of the HC border, two sets of simulations were analyzed based on two experiments conducted by Wei et al. (2023). The two numerical experiments were performed with the same initial conditions in the Community Earth System Model version 2 (CESM2; Danabasoglu et al., 2020) with the fully coupled mode. The first simulation, CTR, is the existing standard CESM2 default setting, where OSA for incident direct radiation is only a function of SZA (Briegleb et al., 1986) and OSA for diffuse radiation is fixed at 0.06, across two partitioned spectral ranges, (0.2–0.7 μm [ultraviolet/visible] and >0.7μm [near infrared]; Neale et al., 2012; Zhao et al., 2021). Therefore, the direct and diffuse OSAs do not change with wavelength, surface wind speed, or the optical properties of ocean surface-layer hydrosols. The modified model run (MDR), implements a comprehensive OSA method that incorporates the comprehensive physical processes for both incoming direct and diffuse beams, and accounts for the spectral dependency of OSA (Wei et al., 2021). Surface albedo treatments of other CESM2 elements, such as land and sea ice, retain the default settings. Simulations contain 32 vertical atmospheric layers on a 1.9° latitude by 2.5° longitude horizontal grid. Each experiment is performed over the 1980–2014 period by specifying historical radiative forcing, as a result, general climate trends are model-generated, along with realistic but not accurately timed large-scale oscillations such as El Niño/Southern Oscillation and the Pacific Decadal Oscillation. The last 30 years of monthly means are analyzed after discarding earlier years as a spin-up period. The detailed experimental configuration is described in Wei et al. (2023).

The comprehensive OSA method implemented in MDR is formulated as a function of SZA, chlorophyll concentration *[chl]*, and the wind field at the ocean surface. SZA determines surface Fresnel reflection (the dominant contribution to OSA), *[chl]* determines light absorption and scattering in the ocean upper layer, and the wind field roughens the sea surface as well as computes the fraction of whitecaps. In CESM2, the OSA is computed within the model coupler. For the implementation of the MDR experiment, the prognostic wind field from the atmospheric model component and the prognostic *[chl]* from the Marine Biogeochemistry Library (MARBL) in the ocean model component of CESM2 are provided to the coupler. Over tropical oceans, the impact of the wind field on the averaged OSA is very weak on the monthly scale since the averaged SZA is low. However, OSA is significantly affected and exhibits greater sensitivity to variations of *[chl]* (Wei et al., 2021).

It is vital to emphasize that the disparities in physical variables between the MDR and CTR are due to intricate feedback mechanisms inherent in the fully coupled CESM2, originating from a subtle adjustment made to the OSA method. Consequently, the movement of the HC subsiding edges in the MDR compared to CTR can be isolated and examined. This is because employing the comprehensive OSA represents the sole external perturbation process in our CESM2 simulations. It is also important to note that this study is motivated to examine time-averaged climate state differences (not a time series trend) attributed to different OSA methods under two distinct experimental setups because both experiments use the same forcing and initial conditions. It is worth noting that this study does not seek to quantify climate responses to OSA changes caused by individual parameters, such as evaluating factorial experiments with static or fixed *[chl]*, and an active or inactive wind field in the comprehensive OSA, nor does it aim to assess model accuracy by comparing with in situ measurements and satellite observations.

As noted in previous studies (e.g., Kang & Lu, 2012; Schneider & Bordoni, 2008), the NH summer (June–July–August; JJA) HC is typically weak with a diffuse boundary, and is strongly affected by extratropical processes (e.g., Kang & Lu, 2012), which can sometimes lead to difficulties in clearly identifying the cell's edge. This can result in considerable uncertainties when trying to pinpoint the HC subsiding boundary. Therefore, in the present study, we only focus on analyzing the results of boreal winter (December–January–February; DJF) seasons.

2.2. Hadley Cell Edge Latitude Metric

The HC in this study is analyzed as a temporal and zonal mean atmospheric circulation in the tropics, which is characterized by the averaged meridional mass streamfunction (MMS), $\Psi(p,\phi)$, on the latitude-pressure plane, given by (e.g., Davis & Birner, 2013):

$$\overline{[\Psi]}(p,\phi) = \frac{2\pi\, a \cos\phi}{g} \int_0^p \overline{[v]}(p,\phi)\, dp, \tag{1}$$

where p is the surface air pressure (unit: hPa); ϕ is the latitude; a is the mean radius of the Earth (unit: m); g is the gravitational acceleration (unit: m s^{-2}); $\overline{[v]}$ is the meridional wind speed (unit: m s^{-1}); and overbars and square brackets represent zonal and time averaging. In this study, two widely used dynamical metrics associated with the MMS are applied to identify the HC edges, $\phi_{\Psi 500}$ (the latitude of zero meridional mass function at 500 hPa; Hu & Fu, 2007), and $\phi_{\int \Psi_{dp}}$ (the latitude of the zero contour of the vertically averaged MMS between 150and 850 hPa; Davis & Birner, 2016).

3. Results

3.1. OSA, Radiation, and Temperature Differences

Figure 1a shows wintertime climatological mean MDR minus CTR OSA relative differences. In the MDR, the proportion of solar flux reflected at the surface (OSA_{MDR}) is determined in a more detailed form, and the penetrating solar flux is absorbed and scattered by hydrosols and water molecules. Therefore, the net effect on upward radiation results in a lower OSA in the MDR than in the CTR, leading to relative differences of $-20 \sim -25\%$ over most of the oceans. Because CTR has the simplified OSA treatment and presumably larger biases than MDR, this suggests that existing CESM runs overestimate OSA and underestimate SST and tropospheric temperature.

With smaller OSA_{MDR}, less incident flux is reflected and more radiant energy is stored almost everywhere in the ocean, causing positive MDR minus CTR net shortwave flux differences $\Delta\ NSW$ (warm colors in Figure 1c). Although mean OSAs are smaller in MDR than in CTR (Figure 1a), $\Delta\ NSW$ is not positive everywhere at the ocean surface (Figure 1c) mainly due to the MDR minus CTR cloud fraction difference. Cloud and aerosol loadings in the lower atmosphere can substantially modulate the relative proportion of direct and diffuse light and the spectral distribution of the incoming illumination hitting the sea surface (e.g., Wild, 2016). The light attenuation effect from clouds is much stronger than from aerosols owing to the larger mass of liquid or ice cloud particles in the atmosphere. Thus, less low cloud coverage (negative $\Delta\ CLDLOW$ in Figure 1b) in MDR generally produces a reduced proportion of atmospheric light attenuation, indicating more solar flux striking the ocean surface (positive $\Delta\ NSW$ in Figure 1c) compared to CTR. While a reversed and relatively weaker correlation between $\Delta\ CLDLOW$ and $\Delta\ NLW$ (net longwave flux difference; Figure 1d) is found, regions of positive (negative) $\Delta\ CLDLOW$ are closely associated with positive (negative) $\Delta\ NLW$. An enhanced low cloud amount absorbs more surface-emitted longwave radiation and reemits more longwave radiation down to the surface, causing less negative $\Delta\ NLW$ (e.g., Siegel & Dickey, 1986). However, increased low clouds enhance surface downward longwave radiative flux but do not lead to strong $\Delta\ NLW$, because a warmer surface (Figure 1e) also increases surface-emitted upward longwave radiative flux (Hegyi & Taylor, 2018; Persson et al., 2017).

The comprehensive OSA (the MDR experiment) is associated with more solar energy injected in the upper ocean, producing a heating effect on SST. However, SST anomalies show more pronounced warming in the central and eastern equatorial Pacific compared to the western equatorial Pacific (Figure 1e), exhibiting an El Niño-like SST difference in the tropical Pacific (e.g., Collins, 2005; Davis & Birner, 2013; Liu et al., 2005; Lian et al., 2018; Song & Zhang et al., 2014). The El Niño-like SST response in fully coupled climate models is a complex process resulting from the interactions between the atmosphere and the ocean. This response is primarily driven by the weakening of the Pacific Walker circulation (e.g., Knutson & Manabe, 1995; Song & Zhang, 2014; Vecchi et al., 2006; Vecchi & Soden, 2007; Zhang & Song, 2006), leading to reduced surface easterly winds (e.g., Vecchi et al., 2006) and oceanic thermocline shoaling (e.g., Luo et al., 2015; Song & Zhang, 2014). Consistent with these findings, our simulated differences between the MDR and CTR also reveal a similar pattern (Figure S1 in Supporting Information S1). These changes set off feedback loops that promote El Niño-like conditions. In addition, variations in ocean dynamics (Liu et al., 2005), heat uptake and transport (Hu et al., 2022; Luo et al., 2015), physical

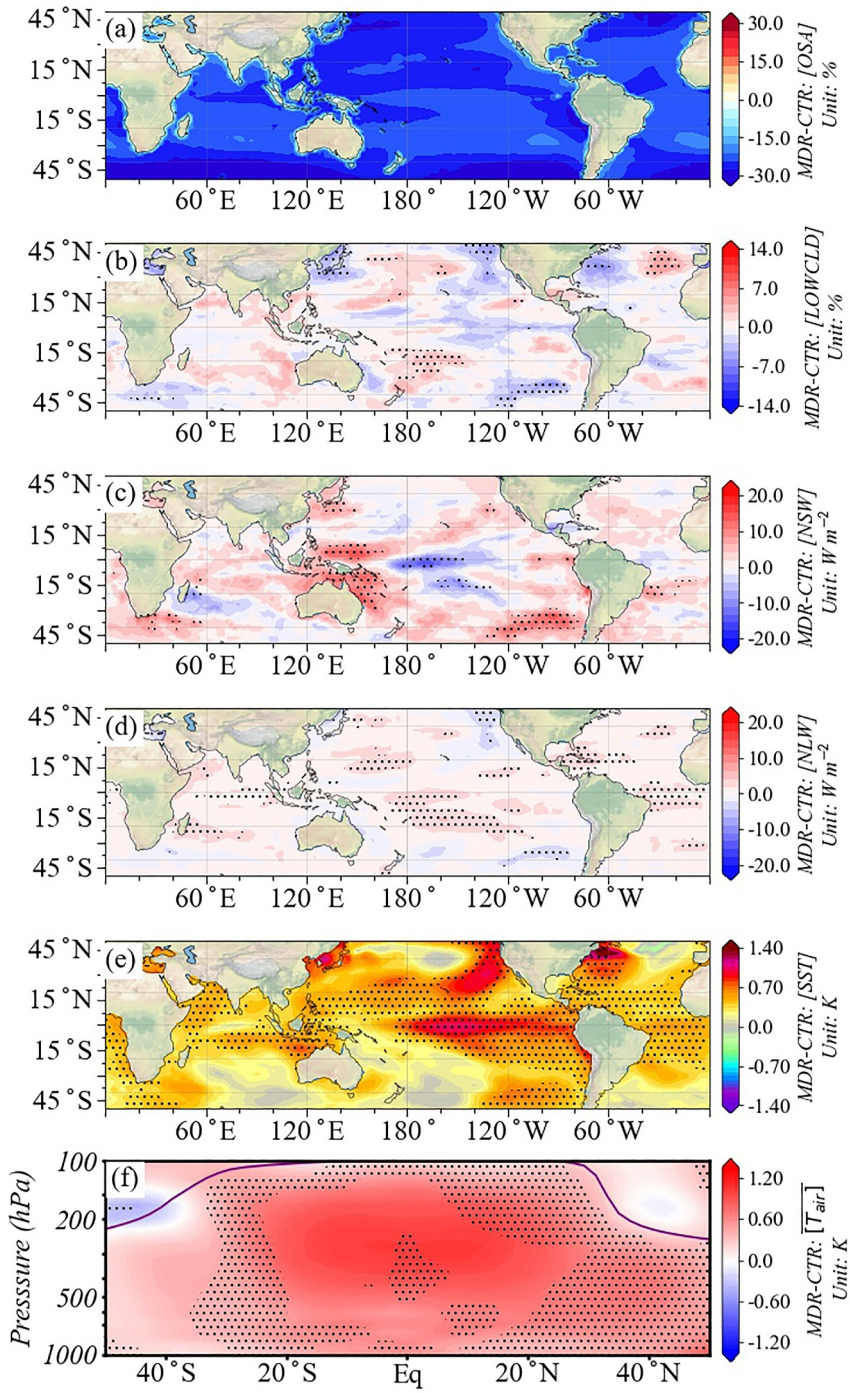

Figure 1. (a): DJF climatological mean MDR minus CTR ocean surface albedo (OSA) difference. (b–f) As in panel (a) but for low cloud fraction (CLDLOW), net shortwave radiative flux (NSW) at the surface, net longwave radiative flux (NLW) at the surface, sea surface temperature (SST), and zonal mean air temperature ($[\overline{T_{\text{air}}}]$). Overbars and square brackets represent zonal and time averaging, respectively. Positive (negative) radiative fluxes represent net downward (upward) energy fluxes. Differences significant at the 95% level are stippled. Purple lines in panel (f) show the CTR mean tropopause pressure. Note: OSA differences here are percentage *relative differences*: $OSA(\%) = 100\times (OSA_{MDR}—OSA_{CTR})/OSA_{CTR}$.

and biogeochemical feedbacks (Eddebbar et al., 2019), and cloud radiative effects (Collins, 2005; Yu & Boer, 2002) can contribute to this El Niño-like SST pattern. Such complex processes of ocean-atmosphere interactions in coupled climate models highlight the need for further research, model evaluations, and analyses of the

Table 1
Long-Term (1985–2014) Mean of the Hadley Cell Subsiding Edge and Its 95% Confidence Level (Montgomery & Runger, 2018) in Each Hemisphere in DJF

Location	Case	Metrics	
		$\overline{[\phi_{500}]}$	$\overline{[\phi_{\int \Psi_{dp}}]}$
NH	CTR	30.38 ± 0.29	30.43 ± 0.28
	MDR	30.17 ± 0.26	30.12 ± 0.22
SH	CTR	−37.37 ± 0.31	−36.76 ± 0.31
	MDR	−37.14 ± 0.37	−36.60 ± 0.36

Note. Negative latitudes are located in the SH. Unit: latitude degrees.

tropical Pacific's response to global warming. We do not present an in-depth analysis of the formation of the El Niño-like SST difference, as it is beyond the scope of this study, but it should be emphasized that the SST anomaly presented here stems from a combination of variations in both surface heat flux and oceanic dynamics, particularly a series of complex air-sea feedbacks within the climate system. In Figure 1f, the warming effect is not confined to the surface but also extends through almost all of the tropical and mid-latitude troposphere. The zonal mean MDR minus CTR air temperature warming is largest in the tropics (20°S–20°N) as a result of the warmer SST pattern and redistributed heat flux release from the ocean to the atmosphere, as suggested by Seager et al. (2003). The accentuated warming in the mid-troposphere can be linked to variations in the quasi-moist adiabatic behavior of the tropical atmosphere in response to increased moist static energy in the boundary layer due to the heat flux changes (Lu et al., 2008).

3.2. Zonal Mean State of HC Subsiding Edge

Table 1 presents time-average meridional statistics of the mean latitude of the HC subsiding edge in both the NH and SH in boreal winter. All HC subsiding fringes using two different HC metrics ($\overline{[\phi_{500}]}$ and $\overline{[\phi_{\int \Psi_{dp}}]}$) are positioned closer to the equator in MDR than in CTR, which means that MDR simulates slightly smaller HC widths (a contraction of the HC). The magnitude of the margin movement (MDR minus CTR) is around 0.16°–0.31° of latitude. The equatorward move of the HC boundary due to an El Niño-like SST change is consistent with previous work (e.g., Adam et al., 2014; Davis & Birner, 2013). However, there are few studies that document in detail the dynamic processes responsible for the HC contraction due to the El Niño-like SST differences, which is the focus of the present study.

3.3. Possible Causes for Movement of the HC Subsiding Edge

3.3.1. Zonal Mean Atmospheric Momentum Perspective

To unravel possible causes of the HC contraction, our approach starts with a zonal mean atmospheric momentum perspective. In the upper troposphere, the temporal and zonal mean momentum equation is obtained by making suitable approximations to the primary equations of momentum (Vallis, 2017). This equation is primarily a balance (ignoring friction as it is small; Cook, 2003) among the absolute vorticity advection, vertical advection, and eddy processes (Vallis, 2017):

$$\underbrace{f\left(1+\overline{[\zeta]}/f\right)\overline{[v]}}_{\text{absolute vorticity advection}}+\underbrace{\overline{[\omega]}\partial_z\overline{[u]}}_{\text{vertical advection}}\approx\underbrace{\partial_y\overline{\left[u'v'\right]}}_{\text{derivative of horizontal eddy momentum flux}}+\underbrace{\partial_z\overline{\left[u'\omega'\right]}}_{\text{derivative of vertical eddy momentum flux}}, \quad (2)$$

where f is the Coriolis parameter with positive (negative) sign in the NH (SH); ζ is the relative vorticity ($\zeta = \partial_y(u\cos\phi)/a\cos\phi$); $\overline{[\zeta]}/f$ is the normalized relative vorticity (dimensionless); and u, v, and ω are the zonal, meridional, and vertical velocities, respectively. The prime represents deviations of velocities from their time-mean values. Subscripts y and z indicate derivatives in latitude and height directions. Terms on the right-hand side of Equation 2 represent derivatives of horizontal and vertical eddy momentum fluxes. The sum of these two terms is the eddy momentum flux divergence (Caballero, 2007; Walker & Schneider, 2006). Overbars and brackets represent zonal and time averaging. Positive (negative) $\overline{[v]}$ indicates air flowing toward the north (south).

In the upper branches of the HC (but not the edges), streamlines (contours in Figure 2a) of the flow are quasi-horizontal (Walker & Schneider, 2006), and therefore the magnitude of the upper meridional velocity $\overline{[v]}$ largely determines how far the horizontal extent of HC can reach. The vertical flow terms in Equation 2 are generally

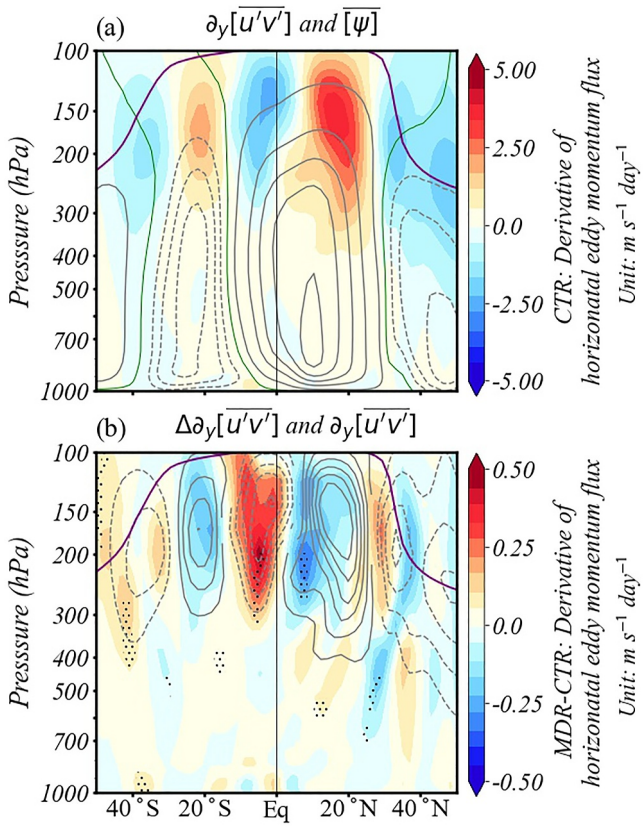

Figure 2. (a) DJF time and zonal mean derivatives of horizontal eddy momentum flux (shaded; $\partial_y[\overline{u'v'}]$) and mean meridional streamfunction (contours; $[\overline{\psi}]$) in CTR. Solid gray contours indicate positive (clockwise) values with a contour interval of 0.4×10^{11} kg s^{-1} ranging from 0.2×10^{11} kg s^{-1} to 1.8×10^{11} kg s^{-1}, dashed contours indicate negative (counterclockwise) values with a contour interval of 0.1×10^{11} kg s^{-1} ranging from -0.35×10^{11} kg s^{-1} to -0.15×10^{11} kg s^{-1}, and the green lines indicate the zero contours. (b) DJF time and zonal mean MDR minus CTR derivative of horizontal eddy momentum flux difference (shaded; $\Delta\ \partial_y[\overline{u'v'}]$). Differences significant at the 95% level are stippled. Solid gray contours ($\partial_y[\overline{u'v'}]$) denote positive derivatives of horizontal eddy momentum flux in CTR and dashed contours ($\partial_y[\overline{u'v'}]$) denote negative values, with a contour interval of 0.5 m s^{-1} day^{-1}. Zero contours are omitted. In each panel, the solid purple line shows the CTR mean tropopause pressure H_e, and the vertical black line is the equator.

weak and can be neglected (see Figures S2b and S2d in Supporting Information S1; Caballero, 2007; Singh & Kuang, 2016; Walker & Schneider, 2006), thus, Equation 2 can be simplified as follows:

$$f(1 + [\overline{\zeta}]/f)[\overline{v}] \approx \partial_y[\overline{u'v'}]. \quad (3)$$

In equatorial regions (about 5°S–5°N), the mean circulation is directly tied to $\partial_y[\overline{u'v'}]$ and $f + [\overline{\zeta}]$ and dynamics should be linked to Equation 3. But in zones such as 5°–35° north or south latitudes, $[\overline{\zeta}]/f$ is negligible (Figure S2a in Supporting Information S1), so the mean circulation is tightly maintained by the balance between the Coriolis Force and the derivative of the horizontal eddy momentum flux, that is, as $[\overline{\zeta}]/f \to 0$, Equation 3 becomes $f[\overline{v}] \approx \partial_y[\overline{u'v'}]$. Any change in $\partial_y[\overline{u'v'}]$ would cause a difference of $[\overline{v}]$.

Because the distribution of solar energy varies with the season, the HC moves seasonally. For instance, during the boreal winter, the northern HC (solid contours in Figure 2a) is much stronger and broader than the southern cell (dashed contours). The descending branches of the two HC cells are associated with subsidence in the subtropics of each hemisphere, indicating the HC edges in the meridional direction. Thus, we may expect to have $[\overline{v}] = 0$ at the poleward edges of the HC, according to $f[\overline{v}] \approx \partial_y[\overline{u'v'}]$, hence $\partial_y[\overline{u'v'}] = 0$ (Ait-Chaalal & Schneider, 2015; Singh & Kuang, 2016; Vallis, 2017). In other words, the locations of the zero derivative of the horizontal eddy momentum flux in both subtropical regions mark the poleward borders of the HC. This attribute is clearly shown in Figure 2a. Specifically, the zero MMS $[\overline{\psi}] = 0$ (the two green lines at the poleward edges of the HC) in the subtropics generally matches the zero boundary of $\partial_y[\overline{u'v'}]$ (shaded in Figure 2a), particularly at levels ranging from 250 to 400 hPa. Those green lines, however, start to deviate from zero values of $\partial_y[\overline{u'v'}]$ as pressure decreases, especially at pressure levels less than 200 hPa in both hemispheres. This is found to be linked to dynamic forcings from the vertical term $\partial_z[\overline{u'\omega'}]$ (relatively small compared to $\partial_y[\overline{u'v'}]$) in Equation 2 at the fringes between the troposphere and the stratosphere (Figure S2d in Supporting Information S1). Nevertheless, the derivative of horizontal eddy momentum flux $\partial_y[\overline{u'v'}]$ is the major driver adjusting the magnitude of the meridional flow $[\overline{v}]$, which in turn largely manages the horizontal poleward orientation of the MMS at the upper branch of the troposphere, determining the poleward extent of the HC (Caballero, 2007; Walker & Schneider, 2006).

We further analyze the dominant dynamics associated with the upper branch of the troposphere separately in five latitudinal zones: (a) the SH subtropics-midlatitudes (35°S–15°S); (b) the SH deep tropics (15°S–5°S); (c) the SH equator vicinity (5°S–0°); (d) the NH equator vicinity (0°–5°N); and (e) the NH deep tropics-midlatitudes (5°N–35°N). We found that $\partial_y[\overline{u'v'}]$ exerts a positive impact on $[\overline{v}]$ revealed by the principle of the cancellation of negative signs (individual variable signs are summarized in Table S1 in Supporting Information S1). For instance, in the SH subtropics-midlatitudes regions, positive values of $\partial_y[\overline{u'v'}]$ (warm colors in Figure 2a) work as a positive effect on $[\overline{v}]$, attributed to the relation of $f[\overline{v}] \approx \partial_y[\overline{u'v'}]$ as $[\overline{\zeta}]/f \to 0$ in Equation 3. Specifically, because f and $[\overline{v}]$ in the SH in the upper southern cell of HC both are negative and their signs cancel each other out, the magnitude of $\partial_y[\overline{u'v'}]$ exerts a positive relation to the numerical value of $[\overline{v}]$. A similar analysis can be applied to the northern cell of the HC in the SH deep tropics, where $\partial_y[\overline{u'v'}]$ elicits a positive difference in $[\overline{v}]$, given that the negative signs of f and $\partial_y[\overline{u'v'}]$ counteract each other, with $[\overline{v}]$ maintaining a positive sign (Table S1 in

Supporting Information S1). In the SH equator vicinity, dynamics should be applied to Equation 3. In this case, the $f(1 + \overline{[\zeta]}/f)$ term turns out to be negative, because f is negative, whereas the $1 + \overline{[\zeta]}/f$ term is positive (see Figure S3 and Table S1 in Supporting Information S1). Consequently, the negative nature of $f(1 + \overline{[\zeta]}/f)$ counterbalances the negative sign of $\partial_y\overline{[u'v']}$, resulting in a positive influence of $\partial_y\overline{[u'v']}$ on $\overline{[v]}$. It is found that dynamics act in the same sense in the NH equator vicinity and the NH deep tropics and mid-latitudes. Thus, the $\partial_y\overline{[u'v']}$ term predominantly takes the role of facilitating the growth of $\overline{[v]}$ in the upper troposphere via the temporal and zonal mean momentum equation (Singh & Kuang, 2016).

Figure 2b shows MDR minus CTR derivatives of horizontal eddy momentum flux difference $\Delta\,\partial_y\overline{[u'v']}$ (shaded). Within the tropical belt, solid (dashed) gray lines overlying the blue (red) colors indicate that $\partial_y\overline{[u'v']}$ in MDR is smaller than that in CTR. Hence, a weaker positive effect of the $\partial_y\overline{[u'v']}$ on $\overline{[v]}$ is found in the upper tropospheric HC in MDR, implying that a lower numerical value of $\overline{[v]}$ limits the growth of $\overline{[v]}$, or constrains the HC poleward extension. Therefore, from the perspective of the temporal and zonal-mean momentum dynamic equation, the derivative of horizontal eddy momentum flux $\partial_y\overline{[u'v']}$ mainly explains the major drivers governing the shift of the HC subsiding edges. Despite this, we may further proceed to ask a question: What controls the change of $\partial_y\overline{[u'v']}$ in MDR compared to CTR?

Since the variable $\partial_y\overline{[u'v']}$ is strongly correlated with $\overline{[u]}$ and $\overline{[v]}$, it is reasonable to speculate on the important role of changes in $\overline{[u]}$, which may affect $\partial_y\overline{[u'v']}$ to some extent, and thus alter the position of the HC edge. While $\overline{[u]}$ is maintained by the vertical zonal wind shear $\overline{[u]}_{vs}$, or equivalently, the meridional (equator-to-pole) temperature gradient $\overline{[T_{air}]}_{grad}$ through the thermal wind theory ($f\overline{[u]}_{vs} = p^{-1}R\overline{[T_{air}]}_{grad}$, where R is the gas constant for air; Vallis, 2017). This reflects the critical role of $\overline{[T_{air}]}_{grad}$ in driving atmospheric circulation, as noted in previous studies (e.g., Korty & Schneider, 2008; Levine & Schneider, 2015), and any perturbations in $\overline{[T_{air}]}_{grad}$ are expected to trigger relevant dynamic responses.

Early studies have shown that tropical expansion can occur under both increased (Butler et al., 2011; Frierson et al., 2007) and decreased (Adam et al., 2014) $\overline{[T_{air}]}_{grad}$, a seemingly paradoxical finding. However, Yang et al. (2020), through the analysis of observational data and climate model simulations, identified that the poleward shift in the distribution (or position) of the $\overline{[T_{air}]}_{grad}$, especially around the mid-latitudes, originating from the responses to nonuniform SST warming, serves as the crucial factor in driving tropical expansion. In a more recent study, Yang et al. (2023) demonstrated that both uniform and nonuniform SST warmings, as well as an idealized global cooling experiment, simulated tropical expansion accompanied by the poleward shift of the $\overline{[T_{air}]}_{grad}$, further reinforcing the critical role of the poleward migration of the $\overline{[T_{air}]}_{grad}$ in setting the tropical widening. Despite these new insights, a detailed explanation of the atmospheric dynamical processes through which the migration of the of $\overline{[T_{air}]}_{grad}$ affects the HC edge remains elusive. We therefore attempt, in view of these findings, to provide a more in-depth discussion of the relevant atmospheric dynamical processes in the following subsection.

As discussed in Section 3.1, MDR simulates a warmer climate than CTR because more radiant energy is stored in the ocean, increasing SST but with an uneven spatial distribution. Correspondingly, a chain of air-sea interactions is involved in the MDR minus CTR difference, which gives rise to heterogeneous warming of the air, and alters the pattern of $\overline{[T_{air}]}_{grad}$. Since our MDR experiment simulated a HC contraction (Table 1), we hypothesize that the $\overline{[T_{air}]}_{grad}$ in the MDR would exhibit an equatorward displacement compared to the CTR. The left panel in Figure 3 shows equatorward migration of the mid-latitude $\overline{[T_{air}]}_{grad}$ in the MDR (green solid contours) with respect to the CTR (gray solid contours) in both hemispheres at the pressure levels greater than 200 hPa, supporting our hypothesis and reinforcing the critical role of the $\overline{[T_{air}]}_{grad}$ migration in driving the HC edge, as suggested by Yang et al. (2020, 2023). Additionally, we also found the upward shift of the mid-latitude $\overline{[T_{air}]}_{grad}$ in MDR (green dashed contours) at the pressure levels below 200 hPa. These $\overline{[T_{air}]}_{grad}$ displacements in MDR shape the pattern of $\overline{[T_{air}]}_{grad}$ differences (shaded) between MDR and CTR. In accordance with the $\overline{[T_{air}]}_{grad}$ changes in MDR, the zonal wind shear anomaly $\Delta\,\overline{[u]}_{vs}$ (Figure 3b) increases according to the thermal wind relation (however, this

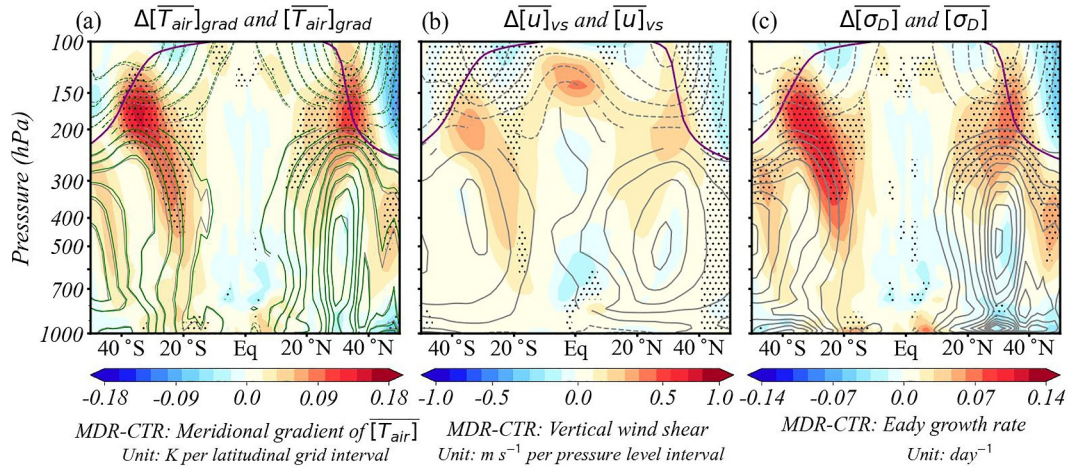

Figure 3. (a) DJF time and zonal mean meridional temperature gradients (gray and green contours represent CTR and MDR, respectively; solid contours indicate positive values, whereas dashed contours indicate negative values. The contours range from −2.3 to 2.3 K per latitudinal grid interval) and MDR minus CTR meridional temperature gradient difference across latitudes (shaded). (b) DJF time and zonal mean vertical zonal wind shear in CTR (contours range from −10.0 to 10.0 m s^{-1} per pressure level interval, with solid lines representing positive values and dashed lines indicating negative values) and MDR minus CTR vertical zonal wind shear difference (shaded). (c) DJF time and zonal mean MDR minus CTR Eady growth rate difference (shaded) and mean Eady growth rate in CTR (contours range from −1.2 day^{s-1} to 2.2 day^{s-1}, with solid lines representing positive values and dashed lines indicating negative values). In each subplot, differences significant at the 95% level are stippled. The solid purple line shows the CTR mean tropopause pressure H_e.

relation fails to explain increased zonal winds at the lower boundary because of additional boundary friction; Vallis, 2017). The zonal wind $[\overline{u}]$ in the MDR is hence intensified as a consequence of the amplification of $[\overline{u}]_{vs}$, manifesting features of stronger westerly winds in the upper section of the troposphere (shading in Figure 4a). Similarly, Figure 4a displays an equatorward shift of $[\overline{u}]$ in the MDR (green solid contours) in both hemispheres, with a notable intensification along their equatorial flanks (bolder shading). This feature is consistent with findings from previous studies (e.g., Lu et al., 2008; Rind et al., 2001; Seager et al., 2003), which have shown that during El Niño (or El Niño-like) events, both observational data and model simulations reveal warming of the

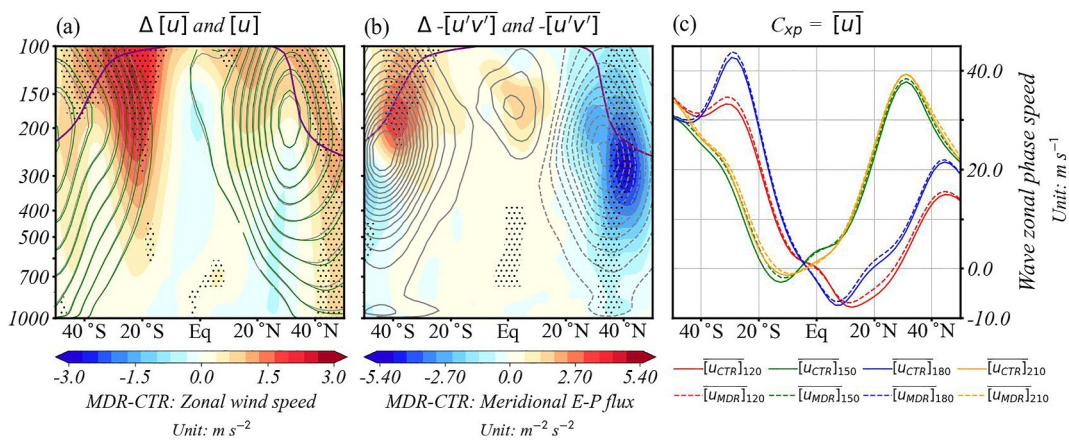

Figure 4. (a) DJF time and zonal mean MDR minus CTR zonal wind difference (shaded) and the mean climatological zonal wind (gray and green contours represent CTR and MDR, respectively. The contours range from 0.0 to 40.0 m s^{-1}, dashed indicate negative values and zero line omitted). (b) DJF time and zonal mean MDR minus CTR meridional E-P flux (shade; equivalently, the reversed horizontal eddy momentum flux) and the meridional climatological E-P flux (solid and dashed contours indicate positive and negative values) in CTR, with a contour interval of 4.0 m^2 s^{-2} from −60.0 to 60.0 m^2 s^{-2}. (c) DJF time and wave zonal phase speed equaling zonal wind at the selected pressure levels across latitudes from both CTR (solid lines) and MDR (dashed lines). In the left and middle subplots, differences that are significant at the 95% level are stippled and the solid purple line shows the mean tropopause pressure H_e in CTR.

tropical atmosphere across latitudes, accompanied by a strengthening of the subtropical jets along their equatorial flanks and a shift toward the equator in both hemispheres.

It is found that the sharpened $\Delta\overline{[u]}_{vs}$ represent a difference due to larger amplitudes of the $\Delta\overline{[T_{air}]}_{grad}$. In these regions, strong velocity shears occur and may be unstable regarding small perturbations (Holton & Gregory, 2013). Mid-latitude planetary waves, or Rossby waves, appear to extract energy and grow as the result of an instability of the mean flow around the jet (Vallis, 2017). This instability is referred to as baroclinic instability (or baroclinicity) and has been extensively characterized in climate systems by the Eady growth rate (e.g., Hoskins & Valdes, 1990; Yin, 2005; Yuval & Kaspi, 2016). The Eady growth rate is proportional to the meridional temperature gradient ($\overline{[\sigma]}_D = 0.31\, gN^{-1}\overline{[T_{air}]}^{-1}\left|\overline{[T_{air}]}_{grad}\right|$, N is the Brunt-Väisälä frequency) or the vertical wind shear via the thermal wind relationship. As noted by Lu et al. (2008), Rossby waves can be thought of as originating from subtropical baroclinic instability, and then propagating away from the source region both equatorward and poleward (as illustrated in Figure 14.13 of Vallis, 2017). During wave propagation, as the zonal wind speed approaches the wave zonal phase speed, $\overline{[u]} - c_p^x \to 0$ in Equation S3 in Supporting Information S1, the term $\frac{\beta}{k^2+l^2}$ approaches zero. In this case, according to Equation S6 in Supporting Information S1, the meridional wave group velocity c_g^y slows down and wave activity hence gradually dissipates. At critical latitudes where the wave zonal phase speed equals the zonal flow ($\overline{[u]} = c_p^x$; such as y_c^N and y_c^S shown in Figure 6.5 of Singh, 2022), the meridional wave group velocity c_g^y equals zero, where meridional Rossby waves break and cannot propagate any further, either poleward or equatorward.

Therefore, increased baroclinic instability in the MDR results from the $\overline{[T_{air}]}_{grad}$ (see positive values of $\Delta\overline{[\sigma]}_D$ in the subtropics in Figure 4c), which favors Rossby wave generation and propagation (Vallis, 2017). The poleward (equatorward) eddy momentum flux is the consequence of equatorward (poleward) Rossby wave propagation. It is worth noting that the horizontal eddy momentum flux, $\overline{[u'v']}$, is equal to the negative value of the meridional component of the *Eliassen-Palm (E-P)* flux ($-\overline{[u'v']}$), as shown in Equation S10 in Supporting Information S1 (Edmon et al., 1980; Vallis, 2017). Figure 4b presents meridional MDR minus CTR E-P flux differences. At upper pressure levels (<200 hPa), solid (dashed) gray lines overlying red (blue) colors mean that the $-\overline{[u'v']}$ in MDR is larger than in CTR, which implies that more E-P flux exists in the upper troposphere, indicating more Rossby wave activity propagates toward the equatorial region in MDR. Figure 4c shows examples of upper-level wave zonal phase speed c_p^x equaling zonal wind $\overline{[u]}$ from both CTR (solid lines) and MDR (dashed lines) in the latitude-phase speed plane. The curve shapes indicate that Rossby waves with slower phase speeds can propagate further into the tropics, while waves with faster phase speeds are restricted to higher latitudes (Lu et al., 2008). The enhanced $\overline{[u]}$ on the equatorial flanks of the subtropical jets (Figure 4a) in the MDR, compared to CTR, draws the critical latitudes (where $\overline{[u]} = c_p^x$) closer to the equator for Rossby waves across all phase speeds. This is reflected by the dashed lines lying above the solid ones (see Figure 4c), aligning with the findings of Lu et al. (2008), where a similar phase speed pattern (the El Niño case above the La Niña case) was simulated in their Figure 9. As a consequence, Rossby wave activities can penetrate deeper into the tropics in MDR compared to CTR. This is consistent with the analysis of the meridional E-P flux variations in Figure 4b. Thus, Rossby wave activity anomalies in the upper troposphere regulate the meridional component of the E-P flux $-\overline{[u'v']}$ (equivalently, modulate the horizontal eddy momentum flux $\overline{[u'v']}$), reshaping the pattern of the derivatives of horizontal eddy momentum flux $\partial_y\overline{[u'v']}$. The changes of $\partial_y\overline{[u'v']}$ hence adjust $\overline{[v]}$ (as discussed in Figure 2), reducing the width of the HC in MDR.

Several studies have identified positive correlations among zonal winds, Rossby waves, and horizontal eddy momentum flux, with particular focus on the equatorial region. For instance, Dima et al. (2005) utilized reanalysis data to examine the tropical zonal momentum balance, finding that equatorward-propagating Rossby waves correlate with an increase in eddy momentum flux, thereby reinforcing zonal wind patterns, especially in the upper tropical atmosphere. Kraucunas and Hartmann (2005), utilizing both climate modeling and reanalysis, demonstrated that equatorial zonal winds are intricately associated with the Rossby wave-induced enhancement of eddy momentum flow in the upper troposphere. Zurita-Gotor and Held (2018) utilized an idealized GCM to investigate the central role of mixed Kelvin-Rossby wave instabilities in the intensification of equatorial zonal

winds. Enhanced Rossby wave activity, along with greater eddy momentum transport, is closely associated with the acceleration of westerlies in the upper troposphere. Although these references did not explicitly discuss the HC edge response, the significant interactions among Rossby waves, eddy momentum transport, and zonal wind patterns in equatorial regions provide essential context and substantiate our comprehensive analysis of meridional wind through these interactions in this subsection.

3.3.2. The Scaling Theory Perspective

Following the previous analysis of HC contraction from the zonal mean momentum perspective, we now explore the movement of the HC edge through a scaling theory to provide a complementary perspective and further confirm the contraction. A widely used analytical scaling, introduced by Held (2000), described the HC boundary as the poleward limit where the angular momentum-conserving (AMC) regime reaches the onset of baroclinic instability (baroclinicity). This scaling has been extensively applied to examine the annual mean state of the HC edge across both idealized and comprehensive climate models (e.g., Chemke et al., 2019; Lu et al., 2007). To further investigate the seasonal variability of the HC edge, Kang and Lu (2012) proposed a revised version of Held's scaling (Held, 2000). Their modification incorporates the location of the ITCZ (ϕ_{ITCZ}), emphasizing the role of convection transferring momentum between the surface and the upper circulation levels. Additionally, they introduced a constant local Rossby number (R_o) to quantify the proximity of the tropical circulation to the inviscid AMC limit, extending the scaling's applicability to the seasonal mean state. Kang and Lu's (2012) scaling has been applied to quantify the influence of the ITCZ on the extent of the HC in response to ocean heat poleward transport in an idealized Aquaplanet GCM (Hilgenbrink & Hartmann, 2018). In this study, we only focus on analyzing the winter HC scaling as formulated by Kang and Lu (2012), which is expressed as:

$$\overline{[\phi_{KL}]} = \left(\frac{1}{2R_o} \left(\overline{[\phi^2_{ITCZ}]} + \sqrt{\overline{[\phi^4_{ITCZ}]} + R_o \cdot \frac{2g \cdot \overline{[\theta_{gds}]} \cdot \overline{[H_0]}}{\Omega^2 \cdot a^2}} \right) \right)^{1/2}, \tag{4}$$

where ϕ_{ITCZ} is the latitude of the ITCZ (unit: degree), defined as the upward velocity-weighted average latitude equatorward of 30°, following Hilgenbrink and Hartmann (2018); θ_{gds} is the gross dry stability (unitless); H_0 is height of the circulation (unit: m); the Earth's angular velocity, Ω, is in unit of $rad\ s^{-1}$. In line with the approaches of Kang and Lu (2012) and Hilgenbrink and Hartmann (2018), the θ_{gds} is defined as $\theta_{gds} = (\theta_2 - \theta_1)/2\Theta$, where θ_2 (unit: K) is the potential temperature at the tropopause pressure, the θ_1 (unit: K) is the potential temperature at 850 hPa, and the Θ (unit: K) is the mean tropospheric potential temperature. The H_0 is given by $H_0 = z_2 - z_1$, where z_2 (unit: m) and z_1 (unit: m) are at the height of the tropopause and the 850 hPa level, respectively. Overbars and brackets represent zonal and time averaging. For scaling, the term $\overline{[\theta_{gds}]} \cdot \overline{[H_0]}$ is averaged over latitude range of 20° N/S ~ 40° N/S for the SH and NH, separately. According to Kang and Lu (2012), the R_o varies depending on the season and hemisphere, but it was determined to be constant across different years, scenarios, and models. Specifically, values of 0.45 for the SH and 1.0 for the NH during DJF were found to provide the best alignment between the scaled $\overline{[\phi_{KL}]}$ and the simulated $\overline{[\phi_{500}]}$ in the ensemble-mean climatology. This conclusion was drawn from an analysis of 20 climate models from the Intergovernmental Panel on Climate Change (IPCC) Fourth Assessment Report (AR4), as reported by Kang and Lu (2012).

As suggested by Kang and Lu (2012), the scaling expression indicates that the dependent variables, including the $\overline{[\phi_{ITCZ}]}$, $\overline{[\theta_{gds}]}$ and $\overline{[H_0]}$, exhibit a strong positive correlation with the $\overline{[\phi_{KL}]}$. Since $\Omega^2 \cdot a^2 \gg 2g \cdot \overline{[\theta_{gds}]} \cdot \overline{[H_0]}$, the contribution of the term $\frac{2g \cdot \overline{[\theta_{gds}]} \cdot \overline{[H_0]}}{\Omega^2 \cdot a^2}$ to the scaling is tiny. This highlights the dominating role of $\overline{[\phi_{ITCZ}]}$ in the scaling, decreases (increases) in $\overline{[\phi_{ITCZ}]}$ are associated with reductions (growths) in $\overline{[\phi_{KL}]}$. In other words, the $\overline{[\phi_{ITCZ}]}$ is closer (further) to the equator, implying the HC contraction (expansion). To quantify the contribution of the ITCZ shift to the movement of the HC edge, we follow the approach outlined by Hilgenbrink and Hartmann (2018). The estimated change in the $\overline{[\phi_{KL}]}$, driven solely by the ITCZ shift, can be calculated as:

Table 2
Long-Term (1985–2014) Mean of the Intertropical Convergence Zone (ITCZ) Location, Difference in the Scaling Relation and Difference in the Scaling Relation Driven by the ITCZ Along With Their 95% Confidence Levels (Montgomery & Runger, 2018) in Each Hemisphere in DJF

	$\overline{[\phi_{\mathrm{ITCZ}}]}$		MDR—CTR	
Location	CTR	MDR	$\Delta\overline{[\phi_{KL}]}$	$\left(\Delta\overline{[\phi_{KI}]}\right)_{\mathrm{ITCZ-driven}}$
NH	—	—	−0.810 ± 0.507	−0.811 ± 0.507
SH	−4.43 ± 0.48	−3.71 ± 0.41	−1.211 ± 0.758	−1.212 ± 0.757

Note. Negative $\overline{[\phi_{\mathrm{ITCZ}}]}$ means the ITCZ is in the SH. while "—" in the NH indicates that the ITCZ is absent in the NH. Unit: latitude degrees. The values in the right two columns are floored to three decimal places to clearly illustrate the differences.

$$\left(\Delta\overline{[\phi_{KI}]}\right)_{ITCZ-driven} \approx \left(\frac{1}{2}\left(\left(\overline{[\phi^2_{ITCZ}]}\right)_{MDR} + \sqrt{\left(\overline{[\phi^4_{ITCZ}]}\right)_{MDR} + \frac{2g\cdot\left(\overline{[\theta_{gds}]}\right)_{CTR}\cdot\left(\overline{[H_0]}\right)_{CTR}}{\Omega^2\cdot a^2}}\right)\right)^{1/2} - \left(\frac{1}{2}\left(\left(\overline{[\phi^2_{ITCZ}]}\right)_{CTR} + \sqrt{\left(\overline{[\phi^4_{ITCZ}]}\right)_{CTR} + \frac{2g\cdot\left(\overline{[\theta_{gds}]}\right)_{CTR}\cdot\left(\overline{[H_0]}\right)_{CTR}}{\Omega^2\cdot a^2}}\right)\right)^{1/2}. \quad (5)$$

As we simulated HC contraction in the MDR compared to the CTR (Table 1), according to the scaling, we assume to have an equatorward displacement of the $\overline{[\phi_{ITCZ}]}$ in the MDR. Table 2 confirms our assumption by showing a more equatorward latitudinal position of the $\overline{[\phi_{ITCZ}]}$ in the MDR. The $\overline{[\phi_{ITCZ}]}$ being closer to the equator in the MDR compared to the CTR corresponds to a contraction of the HC, as indicated by the reduction in $\Delta\overline{[\phi_{KL}]}$ through the scaling relation (Table 2). Here, we do not explore the reasons behind the changes in $\overline{[\phi_{ITCZ}]}$ between the MDR and CTR, as that is beyond the scope of this study, but it should be emphasized that the shift of the $\overline{[\phi_{ITCZ}]}$ originates from a series of feedbacks in the fully coupled model (more detailed mechanisms related the shift of $\overline{[\phi_{ITCZ}]}$ may refer to the literature such as Adam et al., 2016a, 2016b; Hwang et al., 2021; Kang et al., 2018, 2009; Kim et al., 2022; Schneider et al., 2014; Shin et al., 2021; Voigt et al., 2017; Xie et al., 2010). Our focus in this work is solely on analyzing the role of $\overline{[\phi_{ITCZ}]}$ in the scaling relation. Although there are slight increases in both $\overline{[\theta_{gds}]}$ and $\overline{[H_0]}$ in the MDR (Table S2 in Supporting Information S1), the $\left(\Delta\overline{[\phi_{KI}]}\right)_{ITCZ-driven}$ accounts for nearly the entire simulated change in $\Delta\overline{[\phi_{KL}]}$. The ITCZ response of the MDR with respect to the CTR in the scaling can be described as follows: this equatorward movement of the ITCZ location causes the rotation axis, $a\cos(\phi)$, to increase, while the intensified $\overline{[u]}$ on the equatorial flanks of the subtropical jets in the subtropical regions (as shown in Figure 4a), simultaneously enhances the atmospheric angular momentum, $m = (u + \Omega\, a\cos(\phi))\, a\cos(\phi)$. The rise in angular momentum then leads to the AMC zonal wind profile to become baroclinically unstable faster, constraining the extension of the HC edge resulting in a contraction compared to the CTR simulations (Kang & Lu, 2012). This can be also interpreted from another perspective: the equatorward migration of the $\overline{[u]}$ in the MDR results from the equatorward shift of the $\overline{[T_{air}]}_{grad}$ (as discussed in Section 3.3.1), and the corresponding shift of the $\overline{[\sigma]}_D$ in the MDR (as the $\overline{[\sigma]}_D$ is a function of $\overline{[T_{air}]}_{grad}$). Therefore, for the same values of $\overline{[\sigma]}_D$ in CTR and MDR, the location of baroclinicity in the MDR is closer to the equator, leading to a faster onset of baroclinic instability in the AMC zonal wind profile.

To put it briefly, we investigate the intricate relationships between the meridional temperature gradient, zonal winds, Rossby waves, eddy activity (including eddy momentum flux and its derivative), and meridional winds in the equatorial area in order to explore the potential causes of the HC contraction. The scaling theory validates the HC contraction investigation and supports our conclusions.

4. Summary and Discussion

We explored the change of the boreal winter HC subsiding edges (or latitudinal width of the tropical belt) within a fully coupled climate model (CESM2) due to implementing a comprehensive OSA module as an alternative to the existing oversimplified OSA in CESM2. The modified model run (MDR, using the comprehensive OSA), compared to the existing standard OSA module run (CTR) with the same historical forcing scenario and initial conditions simulates warmer boreal winter climatological mean SST with an El Niño-like tropical Pacific SST pattern, and an equatorward move of the HC boundaries. From the temporal and zonal mean momentum dynamic perspective, $\partial_y[\overline{u'v'}]$ in the upper troposphere plays a crucial role in adjusting $[\overline{v}]$, and subsequently affecting the latitudinal positions of the HC subsiding edges, or the width of the tropics. We found equatorward movement of the HC subsiding edges in MDR compared to CTR (equivalent to contraction of the tropics), which is closely correlated with an equatorward migration of $[\overline{T_{air}}]_{grad}$ and increases on the equatorial flanks of the subtropical jets, resembling recent findings (Yang et al., 2020, 2023, who highlighted the critical role of the $[\overline{T_{air}}]_{grad}$ poleward migration in setting the HC widening, while the present work links HC contraction to an equatorward movement of the $[\overline{T_{air}}]_{grad}$). The enhanced $[\overline{T_{air}}]_{grad}$ intensifies subtropical $[\overline{u}]$ and elevates baroclinic instability, which pushes the critical latitudes of Rossby waves toward the equator influencing equatorward Rossby wave propagation and then reshaping the horizontal E-P flux $-[\overline{u'v'}]$ (or equivalently, the horizontal eddy momentum flux $[\overline{u'v'}]$). The pattern of $\partial_y[\overline{u'v'}]$ hence changes as a consequence of the Rossby wave anomaly, which constrains $[\overline{v}]$ via the zonal mean momentum equation regulating the equatorward displacement of the HC outer edge (see the schematic diagram in Figure S4 in Supporting Information S1). In addition, through an analysis of a scaling theory, it shows that the equatorward shift of the ITCZ location in MDR along with the intensified subtropical $[\overline{u}]$, leads to an increase in angular momentum. This increase accelerates the onset of baroclinic instability in the AMC zonal wind profile, thereby constraining the expansion of the HC edge and resulting in a contraction compared to the CTR simulations.

The present results further reinforce the key role of the $[\overline{T_{air}}]_{grad}$ migration in setting the HC edge. This work is a limited preliminary study that exclusively examines two dynamic metrics derived from zonally and vertically averaged MMS based on 30-year historical simulations. The analysis focuses solely on the primary zonal mean state components of the simplified momentum equation in the upper troposphere in conjunction with a scaling relation derived from the assumption of angular momentum conservation, which influences the extent of the HC subsiding edge. We focus on the primary factors in the simplified averaged momentum equation in the upper troposphere that influence the meridional HC velocity and affect the HC extent. However, realistic HC edge changes are more complicated, exhibiting strong regional geographical variability (e.g., Grise et al., 2019; Staten et al., 2018; Yang et al., 2020). Although Yang et al. (2020) found that the regional characteristics of the HC width are primarily determined by the regional variations of the $[\overline{T_{air}}]_{grad}$ displacement, further investigations are required to better understand tropical belt movements in response to both regional and global climate variabilities, particularly in relation to large-scale teleconnections such as El Niño-Southern Oscillation, Pacific Decadal Oscillation and North Atlantic Oscillation. Different metrics reflect distinct perspectives on the HC, which can lead to discrepancies in identifying its boundaries. The discrepancy among different metrics may be mainly attributed to the different heights of troposphere defining by metrics (Davis & Birner, 2017). To gain deeper insights into climate dynamics, particularly in long-term simulations under varying climate forcing scenarios, further research is needed to thoroughly compare these metrics and their implications for detecting HC edges. In addition, continued research, model evaluations, and analyses are necessary to thoroughly investigate the El Niño-like warming response and its associated atmospheric and oceanic climate feedbacks in greater detail. Evaluating model-simulated HC against reanalysis data and observational records is equally important to ensure the accuracy and reliability of the simulations.

We underline that the present study focuses solely on the assessment of the fully coupled CESM2. Conducting similar experiments with other climate models could further elevate the level of knowledge about the role of climate feedbacks in HC dynamics resulting from the implementation of the comprehensive OSA treatment in CESM2. Although our work did not involve the assessment of model accuracy, our simulated results still can be viewed as a further step in exploring the important role of OSA in climate dynamics. Previous findings have highlighted that oversimplified SW radiative fluxes at the ocean surface, resulting from neglecting upper ocean

light attenuation processes, are a significant source of error in climate models and need correction (Lengaigne et al., 2009; Patara et al., 2012). In addition to the necessity of incorporating comprehensive physical processes in the calculation of OSA, other important climate processes may also need to be evaluated for similar comprehensive treatments. We recognize that ensemble approaches, such as conducting dozens of OSA modification experiments and analyzing simulations based on the ensemble mean, can be valuable for conducting comparisons with the CESM2 Large Ensemble project (Danabasoglu et al., 2020; Kay et al., 2015). However, the complex treatment of oceanic optical properties required to compute OSA in the fully coupled CESM2 (Wei et al., 2021) is highly computationally demanding. This constraint has limited our ability to conduct ensemble simulations in the fully coupled mode of CESM2. As highlighted in Section 2.1, this study is a preliminary exploration aimed at investigating the differences in the time-averaged climate state arising from the use of different OSA methods under two distinct experimental setups, both of which apply the same historical forcing and initial conditions. As computational capabilities continue to advance, a continuing future research priority will be the development of simplified, yet sophisticated OSA parameterizations that integrate comprehensive physical mechanisms within climate models. This will facilitate more efficient and robust simulations related to OSA, allowing us to conduct more convincing evaluations.

Data Availability Statement

The Community Earth System Model (CESM) version 2, developed and released by National Center for Atmospheric Research (NCAR; Danabasoglu et al., 2020), is freely accessible to the public. The CESM2 simulated data outputs can be found on Zenodo (Wei et al., 2024).

Acknowledgments
This study was primarily supported by the endowment funds related to the David Bullock Harris Chair in Geosciences at the TAMU College of Art & Sciences (02-512231-10000). QF is partly supported by the NSF Grant AGS-2202812 and the Calvin Professorship in Atmospheric Sciences at the University of Washington. We are grateful to Dr. S. Schroeder who helped edit the manuscript. The computations involved in this study were performed using Texas A&M High Performance Research Computing Facilities.

References

Adam, O., Bischoff, T., & Schneider, T. (2016a). Seasonal and interannual variations of the energy flux equator and ITCZ. Part I: Zonally averaged ITCZ position. *Journal of Climate*, *29*(9), 3219–3230. https://doi.org/10.1175/JCLI-D-15-0512.1

Adam, O., Bischoff, T., & Schneider, T. (2016b). Seasonal and interannual variations of the energy flux equator and ITCZ. Part II: Zonally varying shifts of the ITCZ. *Journal of Climate*, *29*(20), 7281–7293. https://doi.org/10.1175/JCLI-D-15-0710.1

Adam, O., Schneider, T., & Harnik, N. (2014). Role of changes in mean temperatures versus temperature gradients in the recent widening of the Hadley circulation. *Journal of Climate*, *27*(19), 7450–7461. https://doi.org/10.1175/JCLI-D-14-00140.1

Ait-Chaalal, F., & Schneider, T. (2015). Why eddy momentum fluxes are concentrated in the upper troposphere. *Journal of the Atmospheric Sciences*, *72*(4), 1585–1604. https://doi.org/10.1175/JAS-D-14-0243.1

Briegleb, B. P., Minnis, P., Ramanathan, V., & Harrison, E. (1986). Comparison of regional clear-sky albedos inferred from satellite observations and model computations. *Journal of Climate and Applied Meteorology*, *25*(2), 214–226. https://doi.org/10.1175/1520-0450(1986)025<0214:CORCSA>2.0.CO;2

Butler, A. H., Thompson, D. W., & Birner, T. (2011). Isentropic slopes, downgradient eddy fluxes, and the extratropical atmospheric circulation response to tropical tropospheric heating. *Journal of the Atmospheric Sciences*, *68*(10), 2292–2305. https://doi.org/10.1175/JAS-D-10-05025.1

Caballero, R. (2007). Role of eddies in the interannual variability of Hadley cell strength. *Geophysical Research Letters*, *34*(22), 1–6. https://doi.org/10.1029/2007GL030971

Chemke, R., & Polvani, L. M. (2018). Ocean circulation reduces the Hadley cell response to increased greenhouse gases. *Geophysical Research Letters*, *45*(17), 9197–9205. https://doi.org/10.1029/2018GL079070

Chemke, R., & Polvani, L. M. (2019). Exploiting the abrupt $4 \times CO_2$ scenario to elucidate tropical expansion mechanisms. *Journal of Climate*, *32*(3), 859–875. https://doi.org/10.1175/JCLI-D-18-0330.1

Chemke, R., Polvani, L. M., & Deser, C. (2019). The effect of Arctic sea ice loss on the Hadley circulation. *Geophysical Research Letters*, *46*(2), 963–972. https://doi.org/10.1029/2018GL081110

Chen, G., Lu, J., & Sun, L. (2013). Delineating the eddy–zonal flow interaction in the atmospheric circulation response to climate forcing: Uniform SST warming in an idealized aquaplanet model. *Journal of the Atmospheric Sciences*, *70*(7), 2214–2233. https://doi.org/10.1175/JAS-D-12-0248.1

Choi, J., Son, S.-W., Lu, J., & Min, S.-K. (2014). Further observational evidence of Hadley cell widening in the Southern Hemisphere. *Geophysical Research Letters*, *41*(7), 2590–2597. https://doi.org/10.1002/2014GL059426

Collins, M. (2005). El Niño-or La Niña-like climate change? *Climate Dynamics*, *24*(1), 89–104. https://doi.org/10.1007/s00382-004-0478-x

Cook, K. H. (2003). Role of continents in driving the Hadley cells. *Journal of the Atmospheric Sciences*, *60*(7), 957–976. https://doi.org/10.1175/1520-0469(2003)060<0957:ROCIDT>2.0.CO;2

Danabasoglu, G., Lamarque, J. F., Bacmeister, J., Bailey, D. A., DuVivier, A. K., Edwards, J., et al. (2020). The community earth system model version 2 (CESM2). *Journal of Advances in Modeling Earth Systems*, *12*(2), e2019MS001916. https://doi.org/10.1029/2019MS001916

Davis, N., & Birner, T. (2016). Climate model biases in the width of the tropical belt. *Journal of Climate*, *29*(5), 1935–1954. https://doi.org/10.1175/JCLI-D-15-0336.1

Davis, N., & Birner, T. (2017). On the discrepancies in tropical belt expansion between reanalyses and climate models and among tropical belt width metrics. *Journal of Climate*, *30*(4), 1211–1231. https://doi.org/10.1175/JCLI-D-16-0371.1

Davis, N. A., & Birner, T. (2013). Seasonal to multidecadal variability of the width of the tropical belt. *Journal of Geophysical Research: Atmospheres*, *118*(14), 7773–7787. https://doi.org/10.1002/jgrd.50610

Deser, C., Tomas, R. A., & Sun, L. (2015). The role of ocean–atmosphere coupling in the zonal-mean atmospheric response to Arctic sea ice loss. *Journal of Climate*, *28*(6), 2168–2186. https://doi.org/10.1175/JCLI-D-14-00325.1

Dima, I. M., Wallace, J. M., & Kraucunas, I. (2005). Tropical zonal momentum balance in the NCEP reanalyses. *Journal of the Atmospheric Sciences*, *62*(7), 2499–2513. https://doi.org/10.1175/JAS3486.1

Eddebbar, Y. A., Rodgers, K. B., Long, M. C., Subramanian, A. C., Xie, S. P., & Keeling, R. F. (2019). El Niño–like physical and biogeochemical ocean response to tropical eruptions. *Journal of Climate*, *32*(9), 2627–2649. https://doi.org/10.1175/JCLI-D-18-0458.1

Edmon, H. J., Jr., Hoskins, B. J., & McIntyre, M. E. (1980). Eliassen-Palm cross sections for the troposphere. *Journal of the Atmospheric Sciences*, *37*(12), 2600–2616. https://doi.org/10.1175/1520-0469(1980)037<2600:EPCSFT>2.0.CO;2

England, M. R., Polvani, L. M., Sun, L., & Deser, C. (2020). Tropical climate responses to projected Arctic and Antarctic sea-ice loss. *Nature Geoscience*, *13*(4), 275–281. https://doi.org/10.1038/s415-020-0546-9

Feng, J., Li, J., Zhu, J., Li, Y., & Li, F. (2019). The contrasting response of Hadley circulation to different meridional structure of sea surface temperature in CMIP5. *Theoretical and Applied Climatology*, *135*(2), 633–647. https://doi.org/10.1007/s00704-018-2393-9

Frierson, D. M., Lu, J., & Chen, G. (2007). Width of the Hadley cell in simple and comprehensive general circulation models. *Geophysical Research Letters*, *34*(18), 1–5. https://doi.org/10.1029/2007GL031115

Fu, Q., Johanson, C. M., Wallace, J. M., & Thomas, R. (2006). Enhanced mid-latitude tropospheric warming in satellite measurements. *Science*, *312*(5777), 1179. https://doi.org/10.1126/science.1125566

Grise, K. M., & Davis, S. M. (2020). Hadley cell expansion in CMIP6 models. *Atmospheric Chemistry and Physics*, *20*(9), 5249–5268. https://doi.org/10.5194/acp-20-5249-2020

Grise, K. M., Davis, S. M., Simpson, I. R., Waugh, D. W., Fu, Q., Allen, R. J., et al. (2019). Recent tropical expansion: Natural variability or forced response? *Journal of Climate*, *32*(5), 1551–1571. https://doi.org/10.1175/JCLI-D-18-0444.1

Hall, A. (2004). The role of surface albedo feedback in climate. *Journal of Climate*, *17*(7), 1550–1568. https://doi.org/10.1175/1520-0442(2004)017<1550:TROSAF>2.0.CO;2

Hegyi, B. M., & Taylor, P. C. (2018). The unprecedented 2016–2017 Arctic sea ice growth season: The crucial role of atmospheric rivers and longwave fluxes. *Geophysical Research Letters*, *45*(10), 5204–5212. https://doi.org/10.1029/2017GL076717

Held, I. M. (2000). The general circulation of the atmosphere: 2000 program in geophysical fluid dynamics. https://doi.org/10.1575/1912/15

Held, I. M., & Hou, A. Y. (1980). Nonlinear axially symmetric circulations in a nearly inviscid atmosphere. *Journal of the Atmospheric Sciences*, *37*(3), 515–533. https://doi.org/10.1175/1520-0469(1980)037<0515:NASCIA>2.0.CO;2

Hilgenbrink, C. C., & Hartmann, D. L. (2018). The response of Hadley circulation extent to an idealized representation of poleward ocean heat transport in an aquaplanet GCM. *Journal of Climate*, *31*(23), 9753–9770. https://doi.org/10.1175/JCLI-D-18-0324.1

Holton, J., & Gregory, H. (2013). *An introduction to dynamic meteorology* (5th ed.). Elsevier.

Homeyer, C. R., & Bowman, K. P. (2013). Rossby wave breaking and transport between the tropics and extratropics above the subtropical jet. *Journal of the Atmospheric Sciences*, *70*(2), 607–626. https://doi.org/10.1175/JAS-D-12-0198.1

Hoskins, B. J., & Valdes, P. J. (1990). On the existence of storm-tracks. *Journal of the Atmospheric Sciences*, *47*(15), 1854–1864. https://doi.org/10.1175/1520-0469(1990)047<1854:OTEOST>2.0.CO;2

Hu, S., Xie, S. P., & Kang, S. M. (2022). Global warming pattern formation: The role of ocean heat uptake. *Journal of Climate*, *35*(6), 1885–1899. https://doi.org/10.1175/JCLI-D-21-0317.1

Hu, Y., & Fu, Q. (2007). Observed poleward expansion of the Hadley circulation since 1979. *Atmospheric Chemistry and Physics*, *7*(19), 5229–5236. https://doi.org/10.5194/acp-7-5229-2007

Hu, Y., Huang, H., & Zhou, C. (2018). Widening and weakening of the Hadley circulation under global warming. *Science Bulletin*, *63*(10), 640–644. https://doi.org/10.1016/j.scib.2018.04.020

Hu, Y., Zhou, C., & Liu, J. (2011). Observational evidence for poleward expansion of the Hadley circulation. *Advances in Atmospheric Sciences*, *28*(1), 33–44. https://doi.org/10.1007/s00376-010-0032-1

Hwang, Y. T., Tseng, H. Y., Li, K. C., Kang, S. M., Chen, Y. J., & Chiang, J. C. (2021). Relative roles of energy and momentum fluxes in the tropical response to extratropical thermal forcing. *Journal of Climate*, *34*(10), 3771–3786. https://doi.org/10.1175/JCLI-D-20-0151.1

Kang, S. M. (2020). Extratropical influence on the tropical rainfall distribution. *Current Climate Change Reports*, *6*(1), 24–36. https://doi.org/10.1007/s40641-020-00154-y

Kang, S. M., Frierson, D. M., & Held, I. M. (2009). The tropical response to extratropical thermal forcing in an idealized GCM: The importance of radiative feedbacks and convective parameterization. *Journal of the Atmospheric Sciences*, *66*(9), 2812–2827. https://doi.org/10.1175/2009JAS2924.1

Kang, S. M., & Lu, J. (2012). Expansion of the Hadley cell under global warming: Winter versus summer. *Journal of Climate*, *25*(24), 8387–8393. https://doi.org/10.1175/JCLI-D-12-00323.1

Kang, S. M., Shin, Y., Kim, H., Xie, S. P., & Hu, S. (2023). Disentangling the mechanisms of equatorial Pacific climate change. *Science Advances*, *9*(19), 1–8. https://doi.org/10.1126/sciadv.adf5059

Kang, S. M., Shin, Y., & Xie, S. P. (2018). Extratropical forcing and tropical rainfall distribution: Energetics framework and ocean Ekman advection. *Npj Climate and Atmospheric Science*, *1*(1), 1–10. https://doi.org/10.1038/s4162-017-0004-6

Kang, S. M., Xie, S. P., Shin, Y., Kim, H., Hwang, Y. T., Stuecker, M. F., et al. (2020). Walker circulation response to extratropical radiative forcing. *Science Advances*, *6*(47), 1–8. https://doi.org/10.1126/sciadv.abd3021

Kay, J. E., Deser, C., Phillips, A., Mai, A., Hannay, C., Strand, G., et al. (2015). The community earth system model (CESM) large ensemble project: A community resource for studying climate change in the presence of internal climate variability. *Bulletin of the American Meteorological Society*, *96*(8), 1333–1349. https://doi.org/10.1175/BAMS-D-13-00255.1

Kim, H., Kang, S. M., Kay, J. E., & Xie, S. P. (2022). Subtropical clouds key to Southern Ocean teleconnections to the tropical Pacific. *Proceedings of the National Academy of Sciences*, *119*(34), e2200514119. https://doi.org/10.1073/pnas.2200514119

Kim, H. K., & Lee, S. (2001). Hadley cell dynamics in a primitive equation model. Part II: Nonaxisymmetric flow. *Journal of the Atmospheric Sciences*, *58*(19), 2859–2871. https://doi.org/10.1175/1520-0469(2001)058<2859:HCDIAP>2.0.CO;2

Knietzsch, M. A., Schröder, A., Lucarini, V., & Lunkeit, F. (2015). The impact of oceanic heat transport on the atmospheric circulation. *Earth System Dynamics*, *6*(2), 591–615. https://doi.org/10.5194/esd-6-591-2015

Knutson, T. R., & Manabe, S. (1995). Time-mean response over the tropical Pacific to increased C02 in a coupled ocean-atmosphere model. *Journal of Climate*, *8*(9), 2181–2199. https://doi.org/10.1175/1520-0442(1995)008<2181:TMROTT>2.0.CO;2

Korty, R. L., & Schneider, T. (2008). Extent of Hadley circulations in dry atmospheres. *Geophysical Research Letters*, *35*(23), 1–5. https://doi.org/10.1029/2008GL035847

Kraucunas, I., & Hartmann, D. L. (2005). Equatorial superrotation and the factors controlling the zonal-mean zonal winds in the tropical upper troposphere. *Journal of the Atmospheric Sciences*, *62*(2), 371–389. https://doi.org/10.1175/JAS-3365.1

Lau, W. K., & Kim, K. M. (2015). Robust Hadley circulation changes and increasing global dryness due to CO2 warming from CMIP5 model projections. *Proceedings of the National Academy of Sciences*, *112*(12), 3630–3635. https://doi.org/10.1073/pnas.1418682112

Lau, W. K., & Tao, W. (2020). Precipitation–radiation–circulation feedback processes associated with structural changes of the ITCZ in a warming climate during 1980–2014: An observational portrayal. *Journal of Climate*, *33*(20), 8737–8749. https://doi.org/10.1175/JCLI-D-20-0068.1

Lengaigne, M., Madec, G., Bopp, L., Menkes, C., Aumont, O., & Cadule, P. (2009). Bio-physical feedbacks in the Arctic Ocean using an Earth system model. *Geophysical Research Letters*, *36*(21), 1–5. https://doi.org/10.1029/2009GL040145

Levine, X. J., & Schneider, T. (2015). Baroclinic eddies and the extent of the Hadley circulation: An idealized GCM study. *Journal of the Atmospheric Sciences*, *72*(7), 2744–2761. https://doi.org/10.1175/JAS-D-14-0152.1

Li, Y., Du, M., Feng, J., Xu, F., & Song, W. (2023). Relationships between the Hadley circulation and tropical sea surface temperature with different meridional structures simulated in CMIP6 models. *Frontiers in Marine Science*, *10*, 1145509. https://doi.org/10.3389/fmars.2023.1145509

Lian, T., Chen, D., Ying, J., Huang, P., & Tang, Y. (2018). Tropical Pacific trends under global warming: El Niño-like or La Niña-like? *National Science Review*, *5*(6), 810–812. https://doi.org/10.1093/nsr/nwy134

Lionello, P., D'Agostino, R., Ferreira, D., Nguyen, H., & Singh, M. S. (2024). The Hadley circulation in a changing climate. *Annals of the New York Academy of Sciences*, *1534*(1), 69–93. https://doi.org/10.1111/nyas.15114

Liu, Z., Vavrus, S., He, F., Wen, N., & Zhong, Y. (2005). Rethinking tropical ocean response to global warming: The enhanced equatorial warming. *Journal of Climate*, *18*(22), 4684–4700. https://doi.org/10.1175/JCLI3579.1

Lu, J., Chen, G., & Frierson, D. M. W. (2008). Response of the zonal mean atmospheric circulation to El Niño versus global warming. *Journal of Climate*, *21*(22), 5835–5851. https://doi.org/10.1175/2008JCLI2200.1

Lu, J., Vecchi, G. A., & Reichler, T. (2007). Expansion of the Hadley cell under global warming. *Geophysical Research Letters*, *34*(6), 1–5. https://doi.org/10.1029/2006GL028443

Lucas, C., Timbal, B., & Nguyen, H. (2014). The expanding tropics: A critical assessment of the observational and modeling studies. *Wiley Interdisciplinary Reviews: Climate Change*, *5*(1), 89–112. https://doi.org/10.1002/wcc.251

Luo, Y., Lu, J., Liu, F., & Liu, W. (2015). Understanding the El Niño-like oceanic response in the tropical Pacific to global warming. *Climate Dynamics*, *45*(7–8), 1945–1964. https://doi.org/10.1007/s00382-014-2448-2

Montgomery, D. C., & Runger, G. C. (2018). *Applied statistics and probability for engineers* (7th ed.). John Wiley and Sons.

Neale, R. B., Chen, C.-C., Gettelman, A., Lauritzen, P. H., Park, S., Williamson, D. L., et al. (2012). Description of the NCAR community atmosphere model (CAM 5.0). Retrieved from https://www.cesm.ucar.edu/models/cesm1.0/cam/docs/description/cam5_desc.pdf

Nguyen, H., Evans, A., Lucas, C., Smith, I., & Timbal, B. (2013). The Hadley circulation in reanalyses: Climatology, variability, and change. *Journal of Climate*, *26*(10), 3357–3376. https://doi.org/10.1175/JCLI-D-12-00224.1

Patara, L., Vichi, M., Masina, S., Fogli, P. G., & Manzini, E. (2012). Global response to solar radiation absorbed by phytoplankton in a coupled climate model. *Climate Dynamics*, *39*(7–8), 1951–1968. https://doi.org/10.1007/s00382-012-1300-9

Persson, P. O. G., Shupe, M. D., Perovich, D., & Solomon, A. (2017). Linking atmospheric synoptic transport, cloud phase, surface energy fluxes, and sea-ice growth: Observations of midwinter SHEBA conditions. *Climate Dynamics*, *49*(4), 1341–1364. https://doi.org/10.1007/s00382-016-3383-1

Rind, D., Chandler, M., Lonergan, P., & Lerner, J. (2001). Climate change and the middle atmosphere: 5. Paleostratosphere in cold and warm climates. *Journal of Geophysical Research*, *106*(D17), 20195–20212. https://doi.org/10.1029/2000JD900548

Rollings, M., & Merlis, T. M. (2021). The observed relationship between Pacific SST variability and Hadley cell extent trends in reanalyses. *Journal of Climate*, *34*(7), 2511–2527. https://doi.org/10.1175/JCLI-D-20-0410.1

Schneider, T. (2006). The general circulation of the atmosphere. *Annual Review of Earth and Planetary Sciences*, *34*(1), 655–688. https://doi.org/10.1146/annurev.earth.34.031405.125144

Schneider, T., Bischoff, T., & Haug, G. H. (2014). Migrations and dynamics of the intertropical convergence zone. *Nature*, *513*(7516), 45–53. https://doi.org/10.1038/nature13636

Schneider, T., & Bordoni, S. (2008). Eddy-mediated regime transitions in the seasonal cycle of a Hadley circulation and implications for monsoon dynamics. *Journal of the Atmospheric Sciences*, *65*(3), 915–933. https://doi.org/10.1175/2007JAS2415.1

Seager, R., Harnik, N., Kushnir, Y., Robinson, W., & Miller, J. (2003). Mechanisms of hemispherically symmetric climate variability. *Journal of Climate*, *16*(18), 2960–2978. https://doi.org/10.1175/1520-0442(2003)016<2960:MOHSCV>2.0.CO;2

Seidel, D. J., Fu, Q., Randel, W. J., & Reichler, T. J. (2008). Widening of the tropical belt in a changing climate. *Nature Geosciences*, *1*(1), 21–24. https://doi.org/10.1038/ngeo.2007.38

Seidel, D. J., & Randel, W. J. (2007). Recent widening of the tropical belt: Evidence from tropopause observations. *Journal of Geophysical Research*, *112*(20), 2–7. https://doi.org/10.1029/2007JD008861

Seo, K. H., Frierson, D. M. W., & Son, J. H. (2014). A mechanism for future changes in Hadley circulation strength in CMIP5 climate change simulations. *Geophysical Research Letters*, *41*(14), 5251–5258. https://doi.org/10.1002/2014GL060868

Shin, Y., Kang, S. M., Takahashi, K., Stuecker, M. F., Hwang, Y. T., & Kim, D. (2021). Evolution of the tropical response to periodic extratropical thermal forcing. *Journal of Climate*, *34*(15), 6335–6353. https://doi.org/10.1175/JCLI-D-20-0493.1

Siegel, D. A., & Dickey, T. D. (1986). Variability of net longwave radiation over the eastern North Pacific Ocean. *Journal of Geophysical Research*, *91*(C6), 7657–7666. https://doi.org/10.1029/jc091ic06p07657

Singh, M. S. (2022). The general circulation of the atmosphere. In Course notes. *School of Earth, atmosphere and environment*. Monash University. Retrieved from https://singh.sci.monash.edu/GenCirc/notes/GenCirc_notes.pdf

Singh, M. S., & Kuang, Z. (2016). Exploring the role of eddy momentum fluxes in determining the characteristics of the equinoctial Hadley circulation: Fixed-SST simulations. *Journal of the Atmospheric Sciences*, *73*(6), 2427–2444. https://doi.org/10.1175/JAS-D-15-0212.1

Song, X., & Zhang, G. J. (2014). Role of climate feedback in El Niño–like SST response to global warming. *Journal of Climate*, *27*(19), 7301–7318. https://doi.org/10.1175/JCLI-D-14-00072.1

Stachnik, J. P., & Schumacher, C. (2011). A comparison of the Hadley circulation in modern reanalyses. *Journal of Geophysical Research*, *116*(22), 1–14. https://doi.org/10.1029/2011JD016677

Staten, P. W., Lu, J., Grise, K. M., Davis, S. M., & Birner, T. (2018). Re-examining tropical expansion. *Nature Climate Change*, *8*(9), 768–775. https://doi.org/10.1038/s41558-018-0246-2

Tandon, N. F., Gerber, E. P., Sobel, A. H., & Polvani, L. M. (2013). Understanding Hadley cell expansion versus contraction: Insights from simplified models and implications for recent observations. *Journal of Climate*, *26*(12), 4304–4321. https://doi.org/10.1175/JCLI-D-12-00598.1

Trenberth, K. E., & Stepaniak, D. P. (2003). Seamless poleward atmospheric energy transports and implications for the Hadley circulation. *Journal of Climate*, *16*(22), 3706–3722. https://doi.org/10.1175/1520-0442(2003)016<3706:SPAETA>2.0.CO;2

Vallis, G. K. (2017). *Atmospheric and oceanic fluid dynamics: Fundamentals and large-scale circulation* (2nd ed.). Cambridge University Press.

Vecchi, G. A., & Soden, B. J. (2007). Global warming and the weakening of the tropical circulation. *Journal of Climate*, *20*(17), 4316–4340. https://doi.org/10.1175/JCLI4258.1

Vecchi, G. A., Soden, B. J., Wittenberg, A. T., Held, I. M., Leetmaa, A., & Harrison, M. J. (2006). Weakening of tropical Pacific atmospheric circulation due to anthropogenic forcing. *Nature*, *441*(7089), 73–76. https://doi.org/10.1038/nature04744

Voigt, A., Pincus, R., Stevens, B., Bony, S., Boucher, O., Bellouin, N., et al. (2017). Fast and slow shifts of the zonal-mean intertropical convergence zone in response to an idealized anthropogenic aerosol. *Journal of Advances in Modeling Earth Systems*, *9*(2), 870–892. https://doi.org/10.1002/2016MS000902

Walker, C. C., & Schneider, T. (2006). Eddy influences on Hadley circulations: Simulations with an idealized GCM. *Journal of the Atmospheric Sciences*, *63*(12), 3333–3350. https://doi.org/10.1175/JAS3821.1

Watt-Meyer, O., Frierson, D., & Fu, Q. (2019). Hemispheric asymmetry of tropical expansion under CO2 forcing. *Geophysical Research Letters*, *46*(15), 9231–9240. https://doi.org/10.1029/2019GL083695

Webb, P. (2019). *Introduction to oceanography* (1st ed.). Rebus Community. Retrieved from https://rwu.pressbooks.pub/webboceanography/chapter/13-6-estuaries/

Wei, J., Ren, T., Yang, P., DiMarco, S. F., & Huang, X. (2023). Sensitivity of Arctic surface temperature to including a comprehensive ocean interior reflectance to the ocean surface albedo within the fully coupled CESM2. *Journal of Advances in Modeling Earth Systems*, *15*(12), e2023MS003702. https://doi.org/10.1029/2023MS003702

Wei, J., Ren, T., Yang, P., DiMarco, S. F., & Mlawer, E. (2021). An improved ocean surface albedo computational scheme: Structure and performance. *Journal of Geophysical Research: Oceans*, *126*(8), 1–19. https://doi.org/10.1029/2020JC016958

Wei, J., Yang, P., & Fu, Q. (2024). Boreal winter Hadley cell contraction in response to the incorporation of a Comprehensive Ocean Surface albedo in CESM2 (2.0) [Dataset]. *Zenodo*. https://doi.org/10.5281/zenodo.14217357

Wild, M. (2016). Decadal changes in radiative fluxes at land and ocean surfaces and their relevance for global warming. *Wiley Interdisciplinary Reviews: Climate Change*, *7*(1), 91–107. https://doi.org/10.1002/wcc.372

Wittman, M. A. H., Charlton, A. J., & Polvani, L. M. (2007). The effect of lower stratospheric shear on baroclinic instability. *Journal of the Atmospheric Sciences*, *64*(2), 479–496. https://doi.org/10.1175/JAS3828.1

Xie, S. P., Deser, C., Vecchi, G. A., Ma, J., Teng, H., & Wittenberg, A. T. (2010). Global warming pattern formation: Sea surface temperature and rainfall. *Journal of Climate*, *23*(4), 966–986. https://doi.org/10.1175/2009JCLI3329.1

Xie, X., Huang, P., Zhou, S., & Zhang, J. (2022). Changes in ENSO-driven Hadley circulation variability under global warming. *Atmospheric Research*, *274*, 1–16. https://doi.org/10.1016/j.atmosres.2022.106220

Yang, H., Lohmann, G., Lu, J., Gowan, E. J., Shi, X., Liu, J., & Wang, Q. (2020). Tropical expansion driven by poleward advancing midlatitude meridional temperature gradients. *Journal of Geophysical Research: Atmospheres*, *125*(16), e2020JD033158. https://doi.org/10.1029/2020JD033158

Yang, H., Lohmann, G., Shi, X., & Müller, J. (2023). Evaluating the mechanism of tropical expansion using idealized numerical experiments. *Ocean-Land-Atmosphere Research*, *2*, 1–13. https://doi.org/10.34133/olar.0004

Yin, J. H. (2005). A consistent poleward shift of the storm tracks in simulations of 21st century climate. *Geophysical Research Letters*, *32*(18), 1–4. https://doi.org/10.1029/2005GL023684

Yu, B., & Boer, G. (2002). The roles of radiation and dynamical processes in the El Niño-like response to global warming. *Climate Dynamics*, *19*(5–6), 539–554. https://doi.org/10.1007/s00382-002-0244-x

Yuval, J., & Kaspi, Y. (2016). Eddy activity sensitivity to changes in the vertical structure of baroclinicity. *Journal of the Atmospheric Sciences*, *73*(4), 1709–1726. https://doi.org/10.1175/JAS-D-15-0128.1

Zhang, M., & Song, H. (2006). Evidence of deceleration of atmospheric vertical overturning circulation over the tropical Pacific. *Geophysical Research Letters*, *33*(12), L12701. https://doi.org/10.1029/2006GL025942

Zhao, M., Cao, L., Duan, L., Bala, G., & Caldeira, K. (2021). Climate more responsive to marine cloud brightening than ocean albedo modification: A model study. *Journal of Geophysical Research: Atmospheres*, *126*(3), 1–18. https://doi.org/10.1029/2020JD033256

Zhou, C., Lu, J., Hu, Y., & Zelinka, M. D. (2020). Responses of the Hadley circulation to regional sea surface temperature changes. *Journal of Climate*, *33*(2), 429–441. https://doi.org/10.1175/JCLI-D-19-0315.1

Zurita-Gotor, P., & Held, I. M. (2018). The finite-amplitude evolution of mixed Kelvin–Rossby wave instability and equatorial superrotation in a shallow-water model and an idealized GCM. *Journal of the Atmospheric Sciences*, *75*(7), 2299–2316. https://doi.org/10.1175/JAS-D-17-0386.1